Supplementary Notes

Programmable Hydrodynamics of Active Particles

Lisa Rohde[1], Gordei Anchutkin[1], Viktor Holubec[2], and Frank Cichos[1,*]

[1] *Molecular Nanophotonics Group, Peter Debye Institute for Soft Matter Physics, Leipzig University, 04103 Leipzig, Germany.*
[2] *Department of Macromolecular Physics, Faculty of Mathematics and Physics,Charles University, 18000 Prague, Czech Republic.* [*] *cichos@physik.uni-leipzig.de*

Contents

S1 Squirmer temperature profiles

The microswimmer is illuminated with a spatially varying light pattern. The particle absorbs the light and creates a non-uniform heat source density $q(\theta)$ that establishes temperature gradients on the surface. These gradients create thermo-osmotic flows that propel the particle through the fluid. The swimming mechanism lies in the interplay between the imposed surface heating and the resulting temperature distribution. The full description of the temperature field inside the particle ($r < a$) with thermal conductivity κ_{in} and outside of the particle ($r > a$) with thermal conductivity κ_{out} will be analytically derived.

S1.1 Analytical derivation of temperature profiles

The temperature distribution in both the sphere and the surrounding medium obeys the steady-state heat equation, also known as the Laplace's equation:

$$\nabla^2 T = 0\,. \tag{S1}$$

This equation follows from the balance between heat conduction and the absence of internal heat sources or sinks within the bulk materials. Without loss of generality, we assume that the particle swims with a speed $U > 0$ along the positive z-axis. Owing to the symmetry of the particle, the temperature profile must be symmetric with respect to the propulsion axis. Consequently, the temperature can depend only on the azimuthal angle θ (measured from the z-axis) and on the distance r from the particle center. In spherical coordinates, the Laplace equation then reads:

$$\frac{1}{r^2}\frac{\partial}{\partial r}\left(r^2\frac{\partial T}{\partial r}\right) + \frac{1}{r^2\sin\theta}\frac{\partial}{\partial\theta}\left(\sin\theta\frac{\partial T}{\partial\theta}\right) = 0\,, \tag{S2}$$

which can be solved by using the separation of variables method. Assuming a solution of the form $T(r,\theta) = R(r)P(\theta)$, two ordinary differential equations are obtained:

$$r^2\frac{d^2R}{dr^2} + 2r\frac{dR}{dr} - l(l+1)R = 0\,, \tag{S3}$$

$$\sin\theta\frac{d}{d\theta}\left(\sin\theta\frac{dP}{d\theta}\right) + l(l+1)\sin^2\theta P = 0\,. \tag{S4}$$

The second equation yields Legendre polynomials $P_l(\cos\theta)$ as solutions. The radial equation has the general solutions:

$$R(r) = Ar^l + Cr^{-(l+1)}\,. \tag{S5}$$

Inside the sphere, $r < a$, the temperature must remain finite as $r \to 0$. This boundary condition constraints the solution to

$$T_{\text{in}} = T_0 + \sum_{l=0}^{\infty} A_l r^l P_l(\cos(\theta))\,, \tag{S6}$$

where the temperature at the particle center is given by $T_0 + A_0$. Outside the sphere, $r > a$, the temperature approaches the ambient temperature T_0 as $r \to \infty$ which gives the solution

$$T_{\text{out}} = T_0 + \sum_{l=0}^{\infty} C_l r^{-(l+1)} P_l(\cos(\theta))\,. \tag{S7}$$

The surface of the particle imposes boundary conditions that ensure both temperature continuity and heat flux balance. The temperature must be continuous across the interface,

$$T_{\text{in}}(a,\theta) = T_{\text{out}}(a,\theta)\,, \tag{S8}$$

and the heat fluxes inside and outside the particle must be balanced according to

$$\kappa_{\text{in}} \frac{\partial T_{\text{in}}}{\partial r} - \kappa_{\text{out}} \frac{\partial T_{\text{out}}}{\partial r} = q(\theta)\,. \tag{S9}$$

Here $q(\theta)$ represents the heat generated at the surface, and κ_{in} and κ_{out} are the thermal conductivities of the particle and the surrounding medium, respectively. We expand the surface heat flux density in terms of Legendre polynomials:

$$q(\theta) = \sum_{l=0}^{\infty} q_l P_l(\cos(\theta))\,. \tag{S10}$$

The expansion coefficients q_l are constrained by the fact that our experimental setup allows only for heating and not cooling, i.e., $q(\theta) \geq 0$ for all θ. Additionally, the integral $2\pi a^2 \int_0^{\pi} q(\theta) \sin\theta \, d\theta = 4\pi a^2 q_0$ gives the overall heating power absorbed by the particle (for details, see Sec. S5), implying $q_0 > 0$.

Applying the boundary conditions yields:

$$A_l a^l = C_l a^{-(l+1)}\,, \tag{S11}$$

$$\kappa_{\text{in}} l A_l a^{l-1} + \kappa_{\text{out}}(l+1) C_l a^{-(l+2)} = q_l\,. \tag{S12}$$

Solving for the coefficients then yields:

$$A_l = \frac{q_l a^{-l+1}}{\kappa_{\text{in}} l + \kappa_{\text{out}}(l+1)}\,, \tag{S13}$$

$$C_l = \frac{q_l a^{l+2}}{\kappa_{\text{in}} l + \kappa_{\text{out}}(l+1)}\,. \tag{S14}$$

The complete temperature solutions are thus: Inside the particle ($r < a$):

$$T_{\text{in}}(r,\theta) = T_0 + \sum_{l=0}^{\infty} \frac{q_l a^{-l+1}}{\kappa_{\text{in}} l + \kappa_{\text{out}}(l+1)} r^l P_l(\cos\theta)\,. \tag{S15}$$

Outside the particle ($r > a$):

$$T_{\text{out}}(r,\theta) = T_0 + \sum_{l=0}^{\infty} \frac{q_l a^{l+2}}{\kappa_{\text{in}} l + \kappa_{\text{out}}(l+1)} r^{-(l+1)} P_l(\cos\theta)\,. \tag{S16}$$

Note that the coefficients A_l and C_l are temperature expansion coefficients, distinct from the squirmer mode amplitudes B_n introduced later. At the particle surface ($r = a$), we have:

$$T(a,\theta) = T_0 + \sum_{l=0}^{\infty} \frac{q_l a}{\kappa_{\text{in}} l + \kappa_{\text{out}}(l+1)} P_l(\cos\theta)\,. \tag{S17}$$

S1.1.1 Quadrupole approximation of heat flux density and temperature fields

For practical microswimmers, we truncate the expansion at $l = 2$. This captures the monopole term ($l = 0$) which corresponds to uniform heating and does not contribute to self-propulsion (q_0); the dipole term ($l = 1$) which presents a linear heating that creates the propulsion velocity (q_1); and the quadrupole term ($l = 2$) which sets the hydrodynamic signatures of the microswimmer (q_2). The quadrupole approximation of heat flux density then equals

$$q(\theta) = q_0 P_0(\cos\theta) + q_1 P_1(\cos\theta) + q_2 P_2(\cos\theta) = q_0 + q_1 \cos\theta + \frac{q_2}{2}(3\cos\theta^2 - 1)\,. \tag{S18}$$

For the temperature inside the particle ($r < a$), we obtain:

$$T_{\text{in}}(r,\theta) = T_0 + \frac{q_0 a}{\kappa_{\text{out}}} + \frac{q_1}{\kappa_{\text{in}} + 2\kappa_{\text{out}}} r\cos\theta + \frac{q_2}{2\kappa_{\text{in}} + 3\kappa_{\text{out}}} \frac{r^2}{a} \frac{1}{2}(3\cos^2\theta - 1)\,. \tag{S19}$$

For the temperature outside the particle ($r > a$), we obtain:

$$T_{\text{out}}(r,\theta) = T_0 + \frac{q_0 a^2}{\kappa_{\text{out}}}\left(\frac{1}{r}\right) + \frac{q_1 a^3}{\kappa_{\text{in}} + 2\kappa_{\text{out}}}\left(\frac{1}{r}\right)^2 \cos\theta + \frac{q_2 a^4}{2\kappa_{\text{in}} + 3\kappa_{\text{out}}}\left(\frac{1}{r}\right)^3 \frac{1}{2}(3\cos^2\theta - 1)\,. \tag{S20}$$

The temperature on the particle surface ($r = a$) is then equal to

$$T(a,\theta) = T_0 + \frac{q_0 a}{\kappa_{\text{out}}} + \frac{q_1 a}{\kappa_{\text{in}} + 2\kappa_{\text{out}}} \cos\theta + \frac{q_2 a}{2\kappa_{\text{in}} + 3\kappa_{\text{out}}} \frac{1}{2}(3\cos^2\theta - 1)\,. \tag{S21}$$

S1.2 Connection to Squirmer model

S1.2.1 Thermo-osmotic slip velocity

A thermo-phoretic active particle swims due to spatially varying temperate patterns on its surface. These gradients induce a slip velocity at the particle-fluid interface through thermo-phoresis. This slip velocity is directly proportional to the tangential temperature gradient:

$$u_s(\theta) = \frac{\chi}{T_0}\nabla_{\|}T(\theta) = \frac{\chi}{T_0}\frac{1}{a}\frac{\partial T}{\partial\theta}\bigg|_{r=a}, \tag{S22}$$

with a being the radius of the microswimmer and T_0 the ambient temperature. The thermo-osmotic mobility coefficient χ describes the interfacial iterations between the solid and the liquid.
From the general surface temperature in Eq. (S17), we obtain:

$$\frac{\partial T}{\partial\theta}\bigg|_{r=a} = \sum_{l=0}^{\infty} \frac{q_l a}{\kappa_{\text{in}} l + \kappa_{\text{out}}(l+1)} \frac{\partial P_l(\cos\theta)}{\partial\theta}\,. \tag{S23}$$

Considering $\frac{\partial P_l(\cos\theta)}{\partial\theta} = -\sin\theta\frac{dP_l(\cos\theta)}{d(\cos\theta)}$, the slip velocity thus becomes:

$$u_s(\theta) = -\sum_{l=0}^{\infty} \frac{\chi}{T_0}\frac{q_l}{\kappa_{\text{in}} l + \kappa_{\text{out}}(l+1)} \sin\theta\frac{dP_l(\cos\theta)}{d(\cos\theta)}\,. \tag{S24}$$

Quadrupole approximation of thermo-osmotic slip velocities Truncating the expansion at $l = 2$, we obtain the first few Legendre polynomials as:

- $P_1(\cos\theta) = \cos\theta$ gives $\frac{\partial P_1}{\partial\theta} = -\sin\theta\,,$
- $P_2(\cos\theta) = \frac{1}{2}(3\cos^2\theta - 1)$ gives $\frac{\partial P_2}{\partial\theta} = -3\cos\theta\sin\theta\,.$

The tangential temperature gradient at the particle surface (r=a) then yields:

$$\frac{\partial T}{\partial\theta}\bigg|_{r=a} = -\frac{q_1 a}{\kappa_{\text{in}} + 2\kappa_{\text{out}}}\sin\theta - \frac{q_2 a}{2\kappa_{\text{in}} + 3\kappa_{\text{out}}}(3\cos\theta\sin\theta)\,. \tag{S25}$$

Using the identity $\cos\theta\sin\theta = \frac{1}{2}\sin(2\theta)$, we obtain:

$$\frac{1}{a}\frac{\partial T}{\partial\theta}\bigg|_{r=a} = -\frac{q_1}{\kappa_{\text{in}} + 2\kappa_{\text{out}}}\sin\theta - \frac{3q_2}{2(2\kappa_{\text{in}} + 3\kappa_{\text{out}})}\sin(2\theta)\,. \tag{S26}$$

The slip velocity then follows from:

$$u_s(\theta) = \frac{\chi}{T_0}\frac{1}{a}\left(-\frac{q_1 a}{\kappa_{\text{in}} + 2\kappa_{\text{out}}}\sin\theta - \frac{q_2 a}{2\kappa_{\text{in}} + 3\kappa_{\text{out}}}(3\cos\theta\sin\theta)\right)\,. \tag{S27}$$

S1.2.2 Squirmer surface velocities

The squirmer model, introduced by Lighthill (1952) [1], describes swimming motion through prescribed surface velocities. The boundary conditions for a spherical swimmer are:

$$u_\theta(r=a,\theta) = \sum_{n=1}^{\infty} B_n V_n(\cos\theta)\,, \tag{S28}$$

$$u_r(r=a,\theta) = 0\,, \tag{S29}$$

where B_n are the squirmer mode amplitudes and $V_n(\cos\theta) = \frac{-2}{n(n+1)}\frac{\partial P_n(\cos\theta)}{\partial\theta} = \frac{2\sin\theta}{n(n+1)}\frac{dP_n(\cos\theta)}{d(\cos\theta)}$.
Comparing the thermo-osmotic slip velocity in Eq. (S24) with the squirmer model, we need:

$$B_n V_n(\cos\theta) = -\frac{\chi}{T_0}\frac{q_n}{\kappa_{\text{in}} n + \kappa_{\text{out}}(n+1)}\sin\theta\frac{dP_n(\cos\theta)}{d(\cos\theta)}\,. \tag{S30}$$

Substituting the expression for V_n:

$$B_n\frac{2\sin\theta}{n(n+1)}\frac{dP_n(\cos\theta)}{d(\cos\theta)} = -\frac{\chi}{T_0}\frac{q_n}{\kappa_{\text{in}} n + \kappa_{\text{out}}(n+1)}\sin\theta\frac{dP_n(\cos\theta)}{d(\cos\theta)}\,. \tag{S31}$$

This yields:

$$B_n = -\frac{\chi}{T_0}\frac{q_n}{\kappa_{\text{in}} n + \kappa_{\text{out}}(n+1)}\frac{n(n+1)}{2}\,. \tag{S32}$$

This establishes the general connection between heat source modes q_n and squirmer modes B_n, with the negative sign arising from the derivatives of the Legendre polynomials.

Quadrupole approximation of squirmer slip velocities Truncating the expansion at $n = 2$ yields the surface velocity of the squirmer model:

$$u_s(\theta) = B_1\sin(\theta) + \frac{1}{2}B_2\sin(2\theta)\,, \tag{S33}$$

with the coefficients

$$B_1 = -\frac{\chi}{T_0}\frac{q_1}{\kappa_{\text{in}} + 2\kappa_{\text{out}}}\,, \tag{S34}$$

$$B_2 = -\frac{3\chi}{T_0}\frac{q_2}{2\kappa_{\text{in}} + 3\kappa_{\text{out}}}\,. \tag{S35}$$

By using the connection between the heat source modes q_1, q_2 and the squirmer modes B_1, B_2 we can rewrite the surface temperature from Eq. (S21) as:

$$\begin{aligned} T(a,\theta) &= T_0 + \frac{T_0 a}{\chi}\left(-B_1\cos\theta - \frac{B_2}{3}\frac{1}{2}(3\cos^2 - 1)\right) + c \\ &= T_0 + \frac{T_0 a}{\chi}\left(-B_1\cos\theta - \frac{B_2}{2}\cos\theta^2 + \frac{B_2}{6}\right) + c\,, \end{aligned} \tag{S36}$$

with $c = \frac{q_0 a}{\kappa_{\text{out}}}$ setting the baseline heating.
The squirmer parameter β is then:

$$\beta = \frac{B_2}{|B_1|} = -\frac{3q_2}{|q_1|}\frac{\kappa_{\text{in}} + 2\kappa_{\text{out}}}{2\kappa_{\text{in}} + 3\kappa_{\text{out}}}\,. \tag{S37}$$

This relationship allows us to control the squirmer behavior by tuning the heat source coefficients q_1 and q_2. With appropriate thermal conductivities, we can achieve desired swimming characteristics.
The swimming speed of the particle follows from the squirmer theory as $U = (2/3)B_1$ which can be rewritten

as

$$U = -\frac{2}{3}\frac{\chi}{T_0}\frac{q_1}{\kappa_{\text{in}} + 2\kappa_{\text{out}}}\,. \tag{S38}$$

The dipole heating contribution, characterized by q_1, is therefore determining the swimming speed.

S1.3 Positivity constraints in the quadrupole approximation

The temperature profile in the quadrupole approximation depends on the multipole heating coefficients q_0, q_1, and q_2. Since the experimental setup only allows for heating and not cooling, the heat flux density $q(\theta)$ and, consequently, the temperature variation $\Delta T(r,\theta) = T(r,\theta) - T_0$ must be positive. The heat flux density can be expanded as

$$q(\theta) = q_0 + q_1\cos\theta + \frac{q_2}{2}(3\cos\theta^2 - 1)\,. \tag{S39}$$

Let us now locate the minimum of $q(\theta)$. We assume forward propulsion along the positive z-axis, and thus $U > 0$ in Eq. (S38), which implies $q_1 < 0$. The derivative of the heat source density,

$$\frac{dq}{d\theta} = -q_1\sin\theta - 3q_2\cos\theta\sin\theta = 0\,, \tag{S40}$$

thus yields critical points at $\theta_{\text{cr}} = 0, \pi$, and at $\theta_{\text{cr}} = \cos^{-1}\left(\frac{-q_1}{3q_2}\right)$, where θ is measured from the positive z-direction.

At $\theta_{\text{cr}} = 0$, the heat source density reads

$$q(\theta_{\text{cr}} = 0) = q_0 + q_1 + q_2 \geq 0\,. \tag{S41}$$

Maximizing the swimming efficiency requires the overall heating q_0 is minimal for given q_1 and q_2 (for details, see Sec. S5), and thus we set $q(\theta_{\text{cr}} = 0) = 0$. This yields the constraint

$$q_0 = -q_1 - q_2\,. \tag{S42}$$

If the position of minimal heating shifts away from $\theta_{\text{cr}} = 0$, it occurs at

$$\theta_{\text{cr}} = \cos^{-1}\left(\frac{-q_1}{3q_2}\right)\,, \tag{S43}$$

for which the corresponding heat source density is given by

$$q\left(\theta_{\text{cr}} = \cos^{-1}\left(\frac{-q_1}{3q_2}\right)\right) = q_0 - \frac{1}{6}\frac{q_1^2}{q_2} - \frac{q_2}{2}. \tag{S44}$$

Imposing $q(\theta_{\text{cr}}) = 0$ yields the relation

$$q_0 = \frac{q_2}{2} + \frac{1}{6}\frac{q_1^2}{q_2}\,, \tag{S45}$$

which implies $q_2 > 0$.

The second derivative of the heat flux density reads:

$$\frac{d^2q}{d\theta^2} = 3q_2 - q_1\cos\theta - 6q_2\cos^2\theta\,. \tag{S46}$$

The condition $\left.\frac{d^2q}{d\theta^2}\right|_{\theta=\theta_{\text{cr}}} > 0$ for a critical point θ_{cr} to be a minimum holds for $\theta_{\text{cr}} = 0$ when $q_2 < -q_1/3$, and for $\theta_{\text{cr}} = \cos^{-1}\left(\frac{-q_1}{3q_2}\right)$ when $q_2 > -q_1/3$.

Hence, two distinct regimes emerge, connecting the monopole (q_0), dipole (q_1), and quadrupole (q_2) contributions to the heat source density:

$$q_2 < \frac{-q_1}{3} \; : \; q_0 = -q_1 - q_2 \,, \tag{S47}$$

$$q_2 > \frac{-q_1}{3} \; : \; q_0 = \frac{q_2}{2} + \frac{1}{6}\frac{q_1^2}{q_2} \,. \tag{S48}$$

According to the relation between the coefficients q_0, q_1, and q_2, we call these regimes linear and non-linear, respectively. The corresponding heat source densities are

$$q_{\mathrm{lin}}(\theta) = (-q_1 - q_2) + q_1 \cos\theta + \frac{q_2}{2}(3\cos\theta^2 - 1) \,, \tag{S49}$$

$$q_{\mathrm{non-lin}}(\theta) = (\frac{q_2}{2} + \frac{1}{6}\frac{q_1^2}{q_2}) + q_1 \cos\theta + \frac{q_2}{2}(3\cos\theta^2 - 1) \,. \tag{S50}$$

In terms of the squirmer coefficients B_1 and B_2, we get:

$$B_2 > -\frac{\kappa_{\mathrm{in}} + 2\kappa_{\mathrm{out}}}{2\kappa_{\mathrm{in}} + 3\kappa_{\mathrm{out}}} B_1 \; : \; q_0 = -q_1 - q_2 \,, \tag{S51}$$

$$B_2 < -\frac{\kappa_{\mathrm{in}} + 2\kappa_{\mathrm{out}}}{2\kappa_{\mathrm{in}} + 3\kappa_{\mathrm{out}}} B_1 \; : \; q_0 = \frac{q_2}{2} + \frac{q_1^2}{6q_2} \,. \tag{S52}$$

S1.3.1 Temperature fields for constrained heat sources in the quadrupole approximation

With the heat source density constrained by the positivity conditions and by setting $q_1 < 0$ to ensure propulsion in the positive z-direction, explicit expressions for the resulting temperature fields can be derived. The corresponding solutions depend on the specific operating regime considered.

Linear regime: $\mathbf{q_2} < \frac{-\mathbf{q_1}}{\mathbf{3}}$: In the linear regime, the monopole heating q_0 is replaced by $q_0 = -q_1 - q_2$. Substitution fo this expression into the temperature solutions from Eqs. (S19), (S20) and (S21) yields the following results:

$$\begin{aligned}
T_{\mathrm{in}}(r,\theta) &= T_0 + \frac{(-q_1 - q_2)a}{\kappa_{\mathrm{in}}} + \frac{q_1}{\kappa_{\mathrm{out}} + 2\kappa_{\mathrm{out}}} r\cos\theta + \frac{q_2}{2\kappa_{\mathrm{in}} + 3\kappa_{\mathrm{out}}}\frac{r^2}{a}\frac{1}{2}(3\cos^2\theta - 1) \,, \\
T_{\mathrm{out}}(r,\theta) &= T_0 + \frac{(-q_1 - q_2)a^2}{\kappa_{\mathrm{out}}}\left(\frac{1}{r}\right) + \frac{q_1 a^3}{\kappa_{\mathrm{in}} + 2\kappa_{\mathrm{out}}}\left(\frac{1}{r}\right)^2 \cos\theta + \frac{q_2 a^4}{2\kappa_{\mathrm{in}} + 3\kappa_{\mathrm{out}}}\left(\frac{1}{r}\right)^3 \frac{1}{2}(3\cos^2\theta - 1) \,, \\
T(a,\theta) &= T_0 + \frac{(-q_1 - q_2)a}{\kappa_{\mathrm{out}}} + \frac{q_1 a}{\kappa_{\mathrm{in}} + 2\kappa_{\mathrm{out}}}\cos\theta + \frac{q_2 a}{2\kappa_{\mathrm{in}} + 3\kappa_{\mathrm{out}}}\frac{1}{2}(3\cos^2\theta - 1) \,.
\end{aligned} \tag{S53}$$

Non-linear regime: $\mathbf{q_2} > \frac{-\mathbf{q_1}}{\mathbf{3}}$: In the non-linear regime, the monopole heating q_0 is replaced by $q_0 = \frac{q_2}{2} + \frac{q_1^2}{6q_2}$. Substitution fo this expression into the general temperature solutions from Eqs. (S19), (S20) and (S21) yields the following results:

$$\begin{aligned}
T_{\mathrm{in}}(r,\theta) &= T_0 + \frac{(\frac{q_2}{2} + \frac{q_1^2}{6q_2})a}{\kappa_{\mathrm{out}}} + \frac{q_1}{\kappa_{\mathrm{in}} + 2\kappa_{\mathrm{out}}} r\cos\theta + \frac{q_2}{2\kappa_{\mathrm{in}} + 3\kappa_{\mathrm{out}}}\frac{r^2}{a}\frac{1}{2}(3\cos^2\theta - 1) \,, \\
T_{\mathrm{out}}(r,\theta) &= T_0 + \frac{(\frac{q_2}{2} + \frac{q_1^2}{6q_2})a^2}{\kappa_{\mathrm{out}}}\left(\frac{1}{r}\right) + \frac{q_1 a^3}{\kappa_{\mathrm{in}} + 2\kappa_{\mathrm{out}}}\left(\frac{1}{r}\right)^2 \cos\theta + \frac{q_2 a^4}{2\kappa_{\mathrm{in}} + 3\kappa_{\mathrm{out}}}\left(\frac{1}{r}\right)^3 \frac{1}{2}(3\cos^2\theta - 1) \,, \\
T(a,\theta) &= T_0 + \frac{(\frac{q_2}{2} + \frac{q_1^2}{6q_2})a}{\kappa_{\mathrm{out}}} + \frac{q_1 a}{\kappa_{\mathrm{in}} + 2\kappa_{\mathrm{out}}}\cos\theta + \frac{q_2 a}{2\kappa_{\mathrm{in}} + 3\kappa_{\mathrm{out}}}\frac{1}{2}(3\cos^2\theta - 1) \,.
\end{aligned} \tag{S54}$$

S2 Experimental implementation

S2.1 Experimental setup

Our experimental setup comprises an inverted optical microscope (Olympus IX71). The particles are observed using dark field illumination with an oil-immersion dark-field condenser (Olympus, NA 1.2) and an oil-immersion objective (Olympus UPlanApo ×100/0.6). A laser with a wavelength of $\lambda = 532\,\mathrm{nm}$ is built into the optical path. Its wavefront is modulated by a spatial light modulator (SLM) to generate tailored illumination patterns creating the required heat source distributions $q(\theta)$. Figure S**1** shows the optical setup and the sample configuration. Gold nanoparticles (250 nm) trace the hydrodynamic flow field.

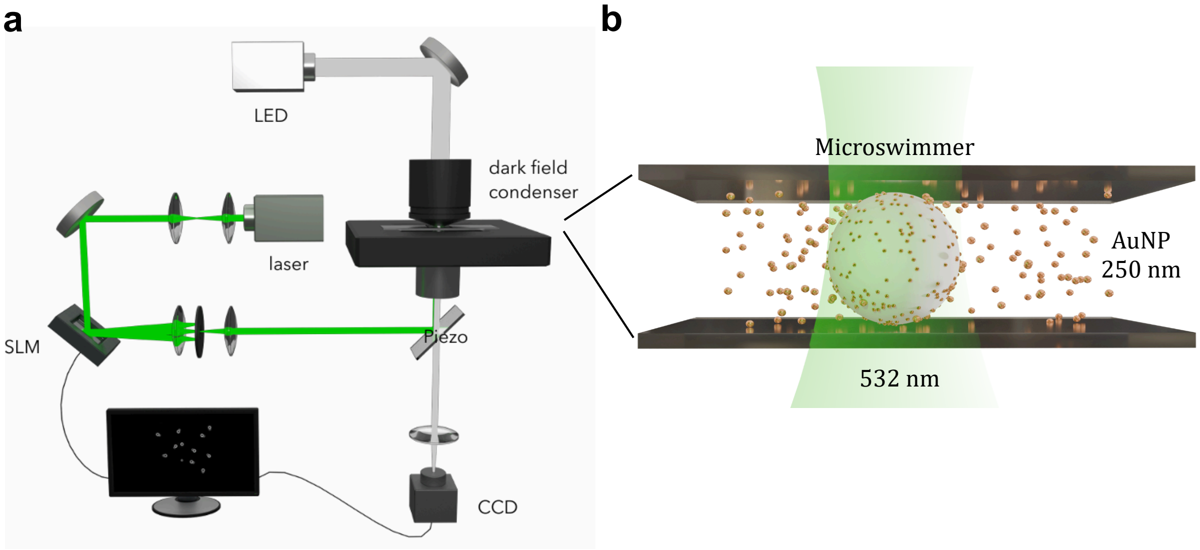

Fig. S1 Experimental setup. a Particle motion is observed with an inverted microscope under dark field illumination. The laser's wavefront is modulated with a spatial light modulator (SLM) to generate distinct illumination patterns. **b** The microswimmer is immobilized between two glass microscope slides. Gold nanoparticles (250 nm) trace the hydrodynamic flow field.

S2.2 Intensity pattern generation

The spatial light modulator (SLM) generates customized illumination patterns to produce the required heat source distribution. Since the absorbed laser intensity is proportional to local heat source density, we must create intensity patterns matching the theoretical $q(\theta)$.

The SLM projects a phase pattern that produces N Gaussian laser spots on the particle surface. To determine an optimized arrangement of these spots, we use a custom algorithm, illustrated in Fig. S**2**. A Monte Carlo optimization algorithm iteratively adjusts spot positions to minimize the mean squared error between realized and target intensity patterns:

$$\mathrm{MSE} = \frac{1}{N_\mathrm{pix}} \sum_{i=1}^{N_\mathrm{pix}} \left(I_i - I_{\mathrm{target},i}\right)^2 \,, \tag{S55}$$

where $I_{\mathrm{target},i} \propto q(\theta_i)$. The optimization terminates when $\mathrm{MSE} < 0.001$ or after 40,000 iterations. The optimized phase image is sent to the SLM. An experimental image of the profile is recorded by utilizing the fluorescence of the dye (Nile Blue A, Sigma-Aldrich) at a wavelength of 532 nm. The MSE of this experimental image is then compared with that of the optimized algorithm-generated image. Next, the number N of Gaussian spots is increased, and the Monte Carlo algorithm is rerun. The value of N that yields an experimental image with the smallest deviation ($\mathrm{MSE} < 10\,\%$) is ultimately selected for the measurements.

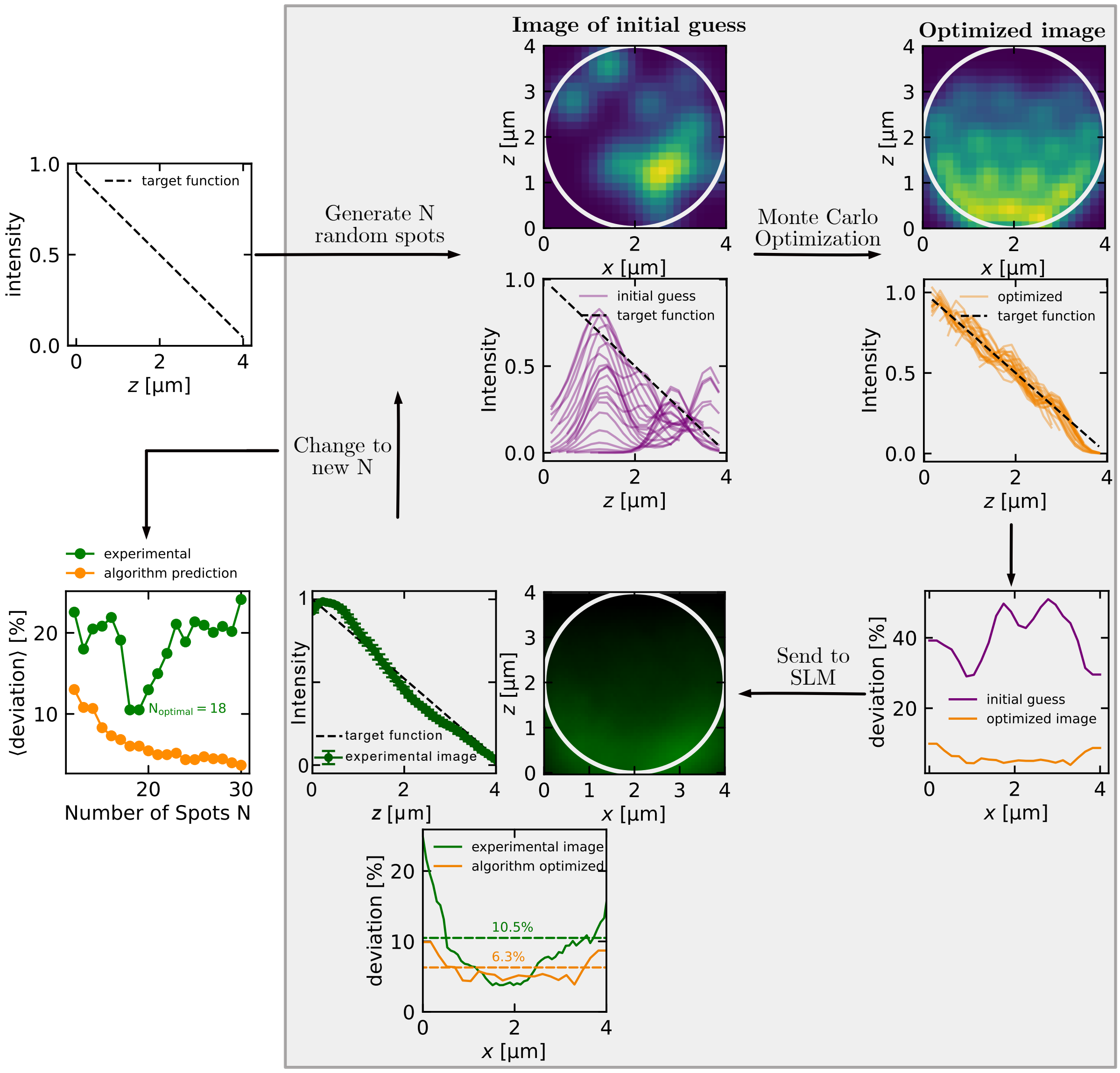

Fig. S2 Intensity pattern generation The SLM projects a phase pattern that produces N Gaussian laser spots on the particle surface. To obtain an optimized spot arrangement, a Monte Carlo algorithm is executed. The resulting optimized phase pattern is then displayed on the SLM, and an experimental image is recorded and analyzed. By varying N, we identify the phase pattern that reproduces the theoretical prediction within a margin of 10 %.

S2.3 Experimental intensity profiles

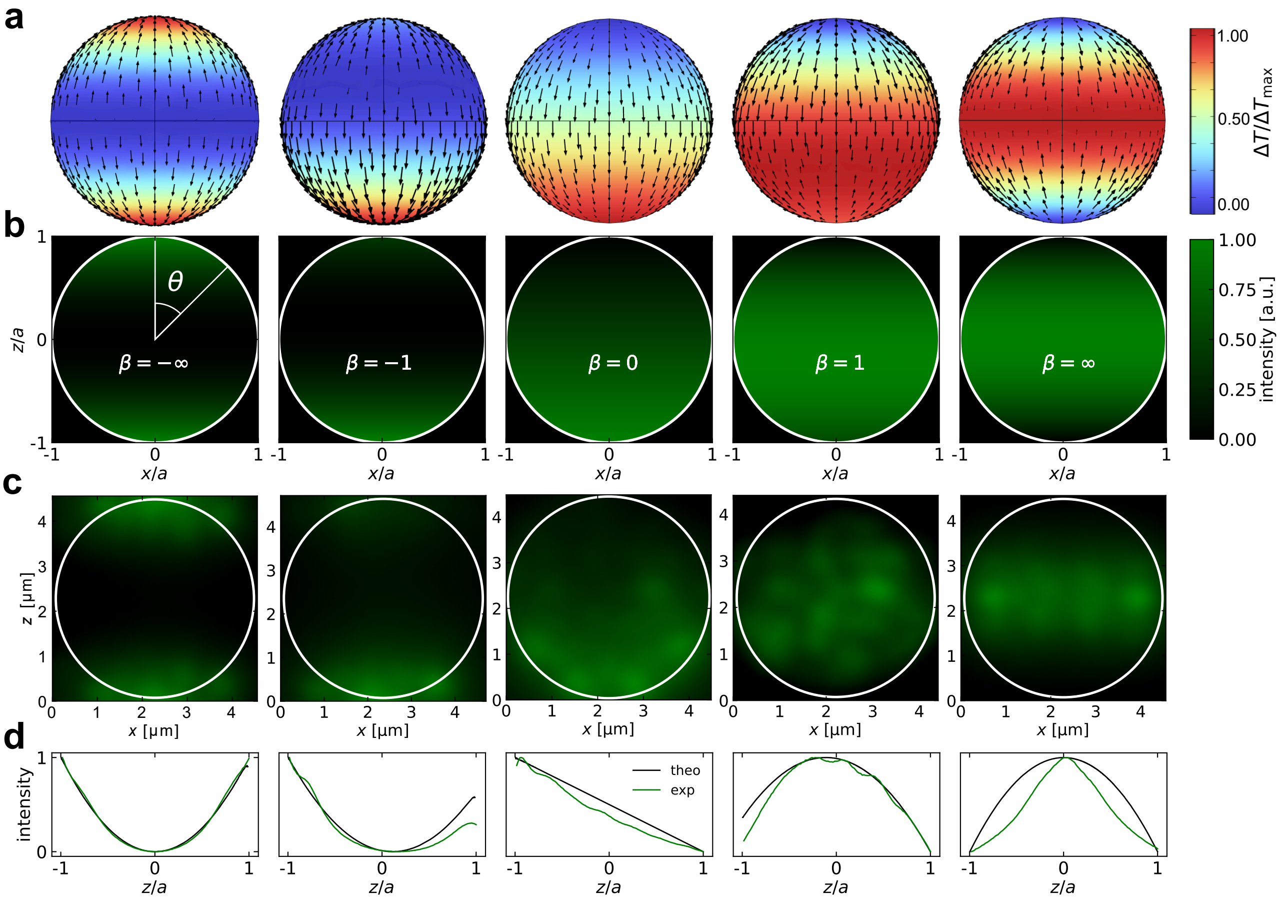

Fig. S3 Boundary flows and intensity profiles for different squirmer parameters. a The simulated boundary flows (black arrows) for different squirmer parameters are determined by the surface temperature distribution which is color coded. **b** Theoretical laser light intensity patterns for different squirmer parameters are computed following Eq. SS36. **c** Microscopy images of the experimental laser fields for different squirmer parameters are shown. They are measured by exploiting the fluorescence of a dye at the wavelength of $\lambda = 523\,\mathrm{nm}$ in the sample plane. **d** The intensity profiles along the z-direction closely align with theoretical predictions indicating precise control over the illumination.

Figure S**3** shows the theoretical and experimental intensity pattern for the negative shaker ($\beta = -\infty$), the pusher ($\beta = \infty$), the neutral squirmer ($\beta = 0$), the puller ($\beta = 1$) and the positive shaker ($\beta = \infty$). The light patterns are recorded by exploiting the fluorescence of the dye (Nile Blue A, Sigma-Aldrich) at a wavelength of $\lambda = 532\,\mathrm{nm}$. The intensity profiles along the z-direction closely align with theoretical predictions indicating precise control over the illumination (cf. Fig. S**3**d).
The simulated boundary flows on the surface of the particle are shown in Fig. S**3**a for different squirmer parameters β. They are determined by the color coded surface temperature profile obtained from a finite element simulation in COMSOL Multiphysics 6.1 by using the heat transfer module and the laminar flow module. Details on the simulation are given in Supplementary Note S4.

S3 Experimental measurements of surface temperatures

In order to get experimental insight into the surface temperature of the illuminated microswimmer, we conducted an experiment in which we immersed the microswimmer in a liquid crystal. Exploiting the phase transition of the liquid crystal at the critical temperature of $T_{\mathrm{PT}} = 308\,\mathrm{K}$, we obtain a reference for estimating the surface temperature in the experiment. When the microswimmer is illuminated by laser light, it will heat up and eventually exceed T_{PT} so that an isotropic phase around the heated particle forms. Due to the refractive index change between the nematic and the isotropic phase, the phase boundary can be observed with an optical microscope under dark-field illumination [2].

Figure S**4** shows a series of microscopy images of two heated shaker squirmers (Fig. S**4**a, $\beta = -\infty$ and Fig. S**4**c, $\beta = \infty$) and of a puller (Fig. S**4**e, $\beta = 1$). With increasing laser light power P, the phase boundary increases. Analyzing the shape of the phase boundary proves the asymmetric temperature profile applied on the surface of the swimmer through laser light illumination. Figure S**4**b,d,f shows the analytical derived two-dimensional temperature profile following Eqs. (S53) and (S54) in a logarithmic color scale for $\beta = \pm\infty, 1$. The experimentally measured white isotherms exhibit excellent agreement with the analytical profile providing evidence for the precise illumination control.

S3.1 Measurement principle

For a quantitative estimate of the surface temperature ΔT_{surf}, we established the following measurement principle. The temperature field outside the particle in the quadrupole approximation (cf. Eq. (S21)) equals to

$$T_{\mathrm{out}}(r,\theta) = T_0 + \frac{q_0 a^2}{\kappa_{\mathrm{out}} r} + \frac{q_1 a^3}{(\kappa_{\mathrm{in}} + 2\kappa_{\mathrm{out}})r^2}\cos\theta + \frac{q_2 a^4}{(2\kappa_{\mathrm{in}} + 3\kappa_{\mathrm{out}})r^3}\frac{1}{2}(3\cos^2\theta - 1)\,. \tag{S56}$$

The phase transition boundary occurs where $T_{\mathrm{out}}(r_{\mathrm{exp}}(\theta),\theta) = T_{\mathrm{PT}}$. This defines an angle-dependent radius $r_{\mathrm{exp}}(\theta)$ where the phase transition occurs:

$$T_{\mathrm{PT}} = T_0 + \frac{q_0 a^2}{\kappa_{\mathrm{out}} r_{\mathrm{exp}}(\theta)} + \frac{q_1 a^3}{(\kappa_{\mathrm{in}} + 2\kappa_{\mathrm{out}})r_{\mathrm{exp}}^2(\theta)}\cos\theta + \frac{q_2 a^4}{(2\kappa_{\mathrm{in}} + 3\kappa_{\mathrm{out}})r_{\mathrm{exp}}^3(\theta)}\frac{1}{2}(3\cos^2\theta - 1)\,. \tag{S57}$$

By measuring the shape of this phase transition boundary $r_{\mathrm{exp}}(\theta)$, we can extract information about the temperature field and validate the heat source distribution parameters q_0, q_1, and q_2.

We can rewrite Eq. (S57) to $T_{\mathrm{PT}} - T_0 = q_0 f_0(r_{\mathrm{exp}}(\theta),\theta) + q_1 f_1(r_{\mathrm{exp}}(\theta),\theta) + q_2 f_2(r_{\mathrm{exp}}(\theta),\theta)$ with the functions

$$f_0(r_{\mathrm{exp}}(\theta),\theta) = \frac{a^2}{\kappa_{\mathrm{out}}\, r_{\mathrm{exp}}(\theta)}\,, \tag{S58}$$

$$f_1(r_{\mathrm{exp}}(\theta),\theta) = \frac{a^3\cos\theta}{(\kappa_{\mathrm{in}} + 2\kappa_{\mathrm{out}})\, r_{\mathrm{exp}}(\theta)^2}\,, \tag{S59}$$

$$f_2(r_{\mathrm{exp}}(\theta),\theta) = \frac{a^4}{(2\kappa_{\mathrm{in}} + 3\kappa_{\mathrm{out}})\, r_{\mathrm{exp}}(\theta)^3}\frac{1}{2}\left(3\cos^2\theta - 1\right)\,. \tag{S60}$$

For each radius r_i and angle θ_i , we define a function $A(r_i,\theta_i)$ as

$$A(r_i,\theta_i) = \begin{bmatrix} f_0(r_i,\theta_i) \\ f_1(r_i,\theta_i) \\ f_2(r_i,\theta_i) \end{bmatrix}^{\mathrm{T}}\,. \tag{S61}$$

For obtaining the individual heating contributions q_0, q_1 and q_2 which make the radius deviate from the spherical shape, we thus have to solve the linear system

$$\mathbf{A}\mathbf{q} = \mathbf{b}\,, \tag{S62}$$

with

$$\mathbf{b} = \begin{bmatrix} T_{\mathrm{PT}} - T_0 \\ T_{\mathrm{PT}} - T_0 \\ \vdots \\ T_{\mathrm{PT}} - T_0 \end{bmatrix} \in \mathbb{R}^N , \tag{S63}$$

where $\mathbf{A} \in \mathbb{R}^{N\times 3}$ is the matrix with rows $A(r_i, \theta_i)$ and $\mathbf{q} \in \mathbb{R}^3$ contains the unknown coefficients (q_0, q_1, q_2). Since $N > 3$, the system is overdetermined and we solve it numerically:

$$\mathbf{q} = (\mathbf{A}^{\mathrm{T}}\mathbf{A})^{-1}\mathbf{A}^{\mathrm{T}}\mathbf{b} . \tag{S64}$$

This approach allows calculation of the monopole (q_0), the dipole (q_1) and quadrupole (q_2) contributions to the heating as a function of the applied laser power for a measured radius $r_{\mathrm{exp}}(\theta)$.

S3.2 Heating contributions and surface temperatures

Figure S**5** shows q_0, q_1 and q_2 as functions of laser power P, extracted from measurements of $r_{\mathrm{exp}}(\theta)$ for the pusher and the neutral squirmer that are presented in the main text and for a puller with $\beta = 1$ (cf. Fig. **6**b). All expansion coefficients increase linearly with laser power P. The dashed lines show fits to the from $q_l = mP$. Inserting the obtained values for q_0, q_1 and q_2 into Eq. (S21) provides the surface temperature for the different swimming modes shown in Fig. S**5**d for a power of $P = 4.35\,\mathrm{mW}$. While the pusher reaches the lowest surface temperatures, with ΔT_{surf} up to $7\,\mathrm{K}$, the neutral squirmer and the puller attain similar higher temperatures, with ΔT_{surf} reaching up to $11 - 13\,\mathrm{K}$. Thermal conductivities of $\kappa_{\mathrm{in}} = 0.03\,\mathrm{W/mK}$ and $\kappa_{\mathrm{out}} = 0.15\,\mathrm{W/mK}$ were used.

Liquid crystal measurements of the positive and negative shaker are presented in Fig. S**6**d-g. The angular variation of $r_{\mathrm{exp}}(\theta)$ confirms the presence of an asymmetric temperature profile induced on the swimmer's surface by the laser illumination further validating our approach to creating controlled swimming modes.

In the experimental system, a nearby wall (cf. Fig. S**6**a) significantly alters the temperature distribution generated by the heated microswimmer [3]. To account for this, numerical simulations were carried out to establish a correction factor linking the temperature increments measured experimentally in 5CB to those expected for a heated particle adjacent to a boundary in water. From these simulation, the relation $\Delta T_{\mathrm{5CB}} = 2.31\,\Delta T_{\mathrm{surf}}$ was obtained with the correction factor of 2.31 representing the numerically derived correction [4].

S4 Simulation of hydrodynamic flow fields

Finite element simulations in COMSOL Multiphysics 6.1 validate the experimentally measured flow fields. The heat transfer module and the laminar flow module were used for simulating flow fields of different squirmers. The simulation domain consists of three cylinders, with two large glass cylinders defining its boundaries (diameter of 40 µm) and a central water domain containing a glass sphere with radius $a = 2.2\,\mu\mathrm{m}$. We apply slip boundary conditions with the dimensionless slip coefficient of $\sigma_{\mathrm{T}} = 0.001$ on all boundaries. Temperature profiles from Eq. (S36) are applied for different squirmer parameters. The resulting velocity fields shown in the main text demonstrate the expected pusher, puller and neutral squirmer modes.

S5 Swimming efficiency

The swimming efficiency was introduced by Lighthill as the ratio of the output power to the input power [1]. The output power involves the sum of all viscous losses causing the directed motion and is calculated by taking the power required to pull a colloidal particle of the same radius a as the swimmer in a liquid of viscosity η. The power required to drag this particle is then related to the Stokes' friction F_{stokes} of this colloid and the swimmer's velocity U:

$$\epsilon = \frac{P_{out}}{P_{in}} = \frac{F_{\mathrm{stokes}} U}{P_{\mathrm{in}}} = \frac{6\pi\eta a U^2}{P_{\mathrm{in}}} . \tag{S65}$$

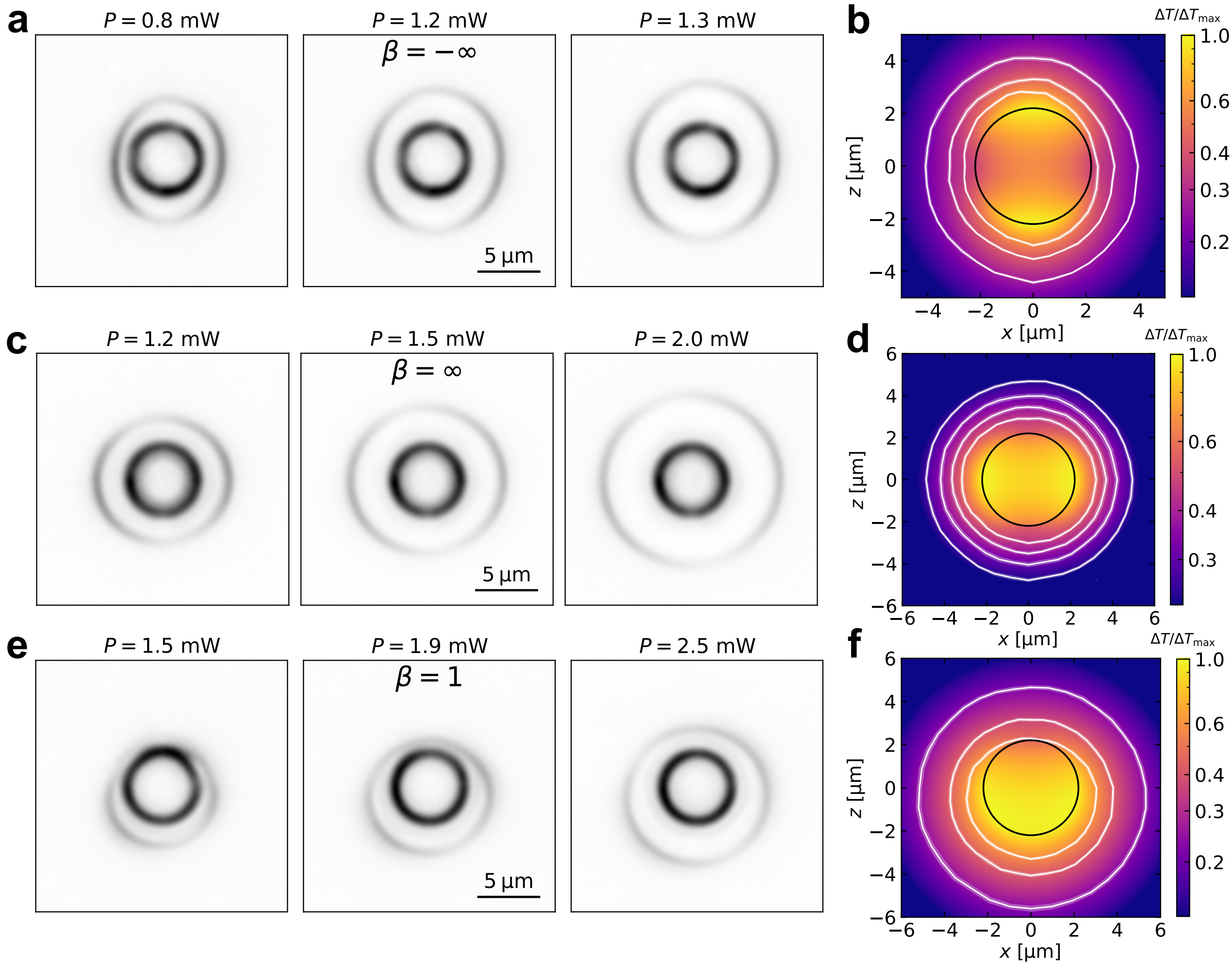

Fig. S4 Liquid crystal phase transitions for different squirmers. a, c, e The series of microscopy images shows the phase boundary of the liquid crystal which increases with increasing laser power P for all squirmer parameters ($\beta = \pm\infty, 1$). The phase boundary is asymmetric around the particle's center following the shape of the illumination profile of the laser light. **b, d, f** The analytical derived two-dimensional temperature field, displayed on a logarithmic color scale, is shown alongside the experimentally measured isotherms, which are indicated in white with shaded regions representing the associated uncertainties. The experimental temperature profile exhibits strong agreement with the theoretical prediction.

The input power relates to the energy absorbed by the particle and involves different processes for different types of swimmers. Here, we have thermo-phoretic swimmers with small gold nanoparticles attached to the surface. By illuminating the particle, each nanoparticle creates a temperature gradient on the surface and contributes to the absorbed power. The input power is therefor the absorbed power by the particle and be expressed as the integral of the heat source density $q(\theta)$ over the sphere's surface:

$$P_{\text{abs}} = \int\int_{\text{sphere}} q(\theta)dS = 2\pi a^2 \int_0^\pi q(\theta)\sin\theta d\theta\,. \tag{S66}$$

Since $\int_0^\pi P_n(\cos(\theta))\sin\theta d\theta = 2\delta_{0n}$, we obtain from the formal expansion (S10) of the heat flux density

$$P_{\text{abs}} = 4\pi a^2 q_0\,. \tag{S67}$$

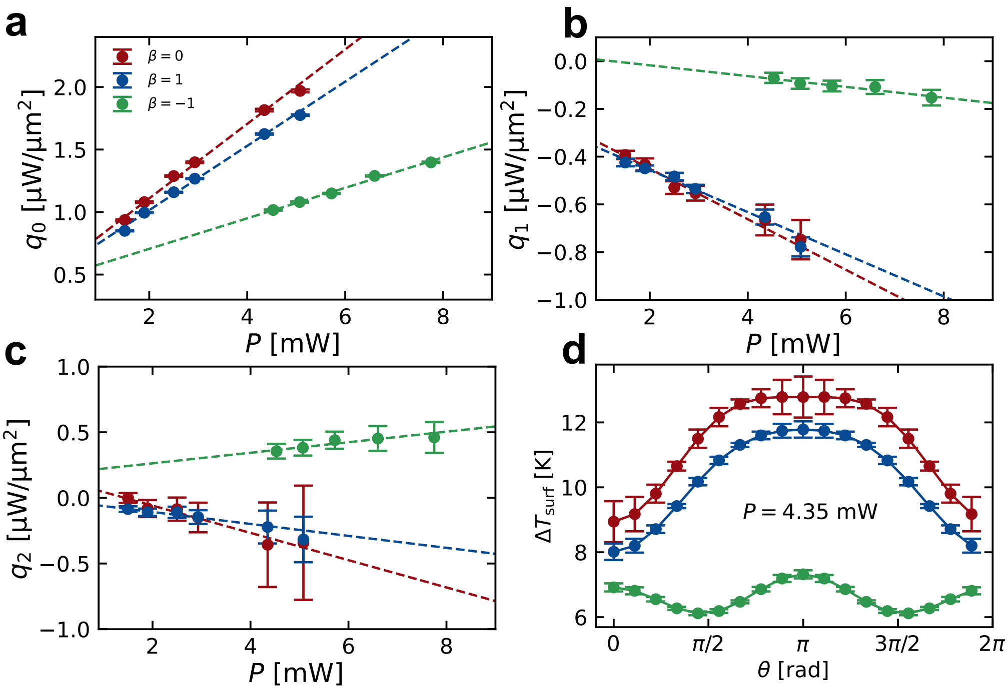

Fig. S5 Heating contributions of squirmers a,b,c Monopole (q_0), dipole (q_1) and quadrupole (q_2) heating contributions as functions of input laser power P for the neutral squirmer ($\beta = 0$), the pusher ($\beta = -1$), and the puller ($\beta = 1$) are extracted from measuring the phase transition radius $r_{\text{exp}}(\theta)$ of an heated microswimmer in a liquid crystal. **d** Using the values for q_0, q_1 and q_2, the surface temperature ΔT_{surf} can be expressed as a function of θ. For the same laser power $P = 4.35\,\text{mW}$, the pusher yields the lowest temperature around 7 K, whereas the puller and neutral squirmer reach higher temperatures of approximately $11 - 13\,\text{K}$.

This expression is valid for arbitrary axially symmetric heating profile. It yields the swimming efficiency

$$\epsilon = \frac{6\pi\eta a U^2}{4\pi a^2 q_0} \tag{S68}$$

$$= \frac{2\eta(\chi/T_0)^2 q_1^2}{3a q_0(\kappa_{\text{in}} + 2\kappa_{\text{out}})} \,. \tag{S69}$$

S5.1 Constraints to swimming efficiency in the quadrupole approximation

The absorbed power depends entirely on the monopole term q_0, which is determined by the positivity constraint: In the **linear regime** ($q_2 < -q_1/3$), the monopole term is constraint to $q_0 = -q_1 - q_2$ which leads to the absorbed power

$$P_{\text{abs,lin}} = 4\pi a^2(-q_1 - q_2) \;\text{ for } q_2 < \frac{-q_1}{3} \,. \tag{S70}$$

In the **non-linear regime** ($q_2 > -q_1/3$), the monopole term is constraint to $q_0 = \frac{q_2}{2} + \frac{q_1^2}{6q_2}$ which leads to the absorbed power

$$P_{\text{abs,non-lin}} = 2\pi a^2\left(\frac{q_1^2}{3q_2} + q_2\right) \;\text{ for } q_2 > \frac{-q_1}{3} \,. \tag{S71}$$

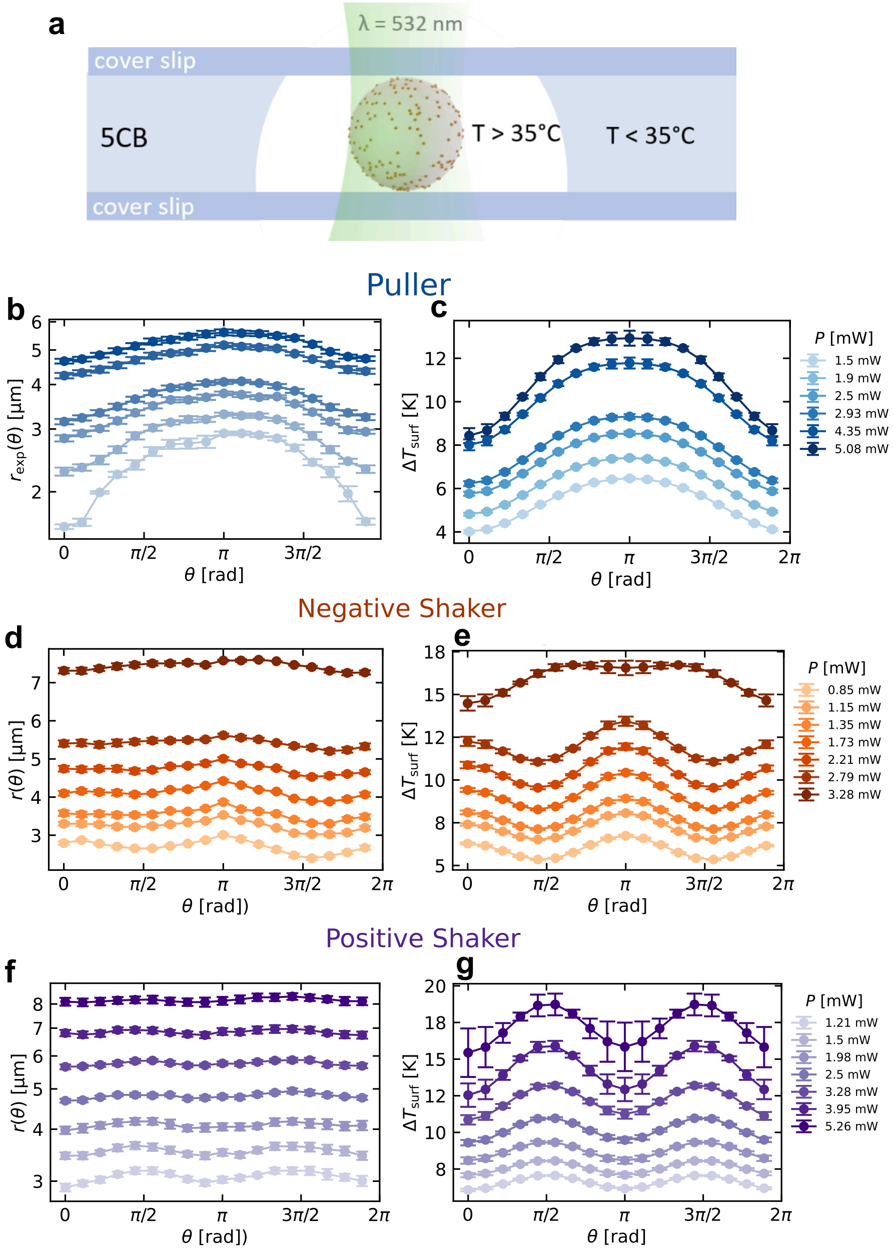

Fig. S6 Measurement of surface temperatures for different squirmers. a The microswimmer is immobilized at the microscope slide and immersed in a liquid crystal (5CB). **b,d,f** The angular variation of the measured phase transition radius $r_{\mathrm{exp}}(\theta)$ reflects the asymmetric temperature fields, shown here for the puller and the negative and positive shaker, respectively. **c,e,g** The corresponding surface temperatures as a function of θ confirm the presence of an asymmetric temperature profile induced on the swimmer's surface by the laser illumination further validating our approach to creating controlled swimming modes.

Based on the above expressions for the absorbed power and on the swimming speed U from Eq. (S38), the corresponding efficiencies for the two regimes are obtained as

$$\epsilon_{\mathrm{lin}} = \frac{6\pi\eta a\left(\frac{2}{3}\frac{\chi}{T_0}\frac{q_1}{\kappa_{\mathrm{in}}+2\kappa_{\mathrm{out}}}\right)^2}{4\pi a^2(-q_1-q_2)} = \frac{2\eta\chi^2}{3aT_0^2(\kappa_{\mathrm{in}}+2\kappa_{\mathrm{out}})^2}\frac{q_1^2}{(-q_1-q_2)}\,, \tag{S72}$$

$$\epsilon_{\mathrm{non-lin}} = \frac{6\pi\eta a\left(\frac{2}{3}\frac{\chi}{T_0}\frac{q_1}{\kappa_{\mathrm{in}}+2\kappa_{\mathrm{out}}}\right)^2}{2\pi a^2(\frac{q_1^2}{3q_2}+q_2)} = \frac{4\eta\chi^2}{3aT_0^2(\kappa_{\mathrm{in}}+2\kappa_{\mathrm{out}})^2}\frac{q_1^2}{(\frac{q_1^2}{3q_2}+q_2)}\,. \tag{S73}$$

The expressions indicate that the efficiency depends solely on the dipole (q_1) and quadrupole (q_2) heating contributions. As described in Sec. S3, these quantities can be extracted from the temperature measurements using the phase transition of a liquid crystal.

S5.2 Maximum swimming efficiency in the quadrupole approximation

Figure 4d in the main paper shows the absorbed power in both regimes for a fixed dipole heating value $q_1 = -0.4\,\mu\mathrm{W}\,(\mu\mathrm{m})^{-1}$ as a function of the squirmer parameter β. The value of q_1 fixes the swimming speed through Eq. (S38). Let us now maximize the efficiency for a given swimming speed $U \propto -q_1 > 0$, and thus a given output power $P_{\mathrm{out}} = 6\pi\eta a U^2$, in the quadrupole approximation. For a speed fixed U, the efficiency (S69) is maximized by minimizing the overall absorbed power and thus q_0.

In the linear regime ($q_2 < -q_1/3$), $q_0 = -q_1 - q_2$ is for a fixed $q_1 < 0$ maximized by taking largest possible $q_2 = -q_1/3$. This gives the maximum efficency and the corresponding squirmer parameter

$$\epsilon^{\star}_{\mathrm{lin}} = \frac{9}{4}\frac{\eta\chi}{aT_0}\frac{U}{\kappa_{\mathrm{in}} + 2\kappa_{\mathrm{out}}}\,, \tag{S74}$$

$$\beta^{\star}_{\mathrm{lin}} = -\frac{\kappa_{\mathrm{in}} + 2\kappa_{\mathrm{out}}}{2\kappa_{\mathrm{in}} + 3\kappa_{\mathrm{out}}}\,. \tag{S75}$$

In the non-linear regime ($q_2 > -q_1/3$), the minimum absorbed power can be determined by solving $\partial P_{\mathrm{abs,non-lin}}/\partial q_2 = \frac{-q_1^2}{3q_2^2} + 1 = 0$ which yields the condition $q_1^2 = 3q_2^2$. Under the conditions $q_1 < 0$ and $q_2 > 0$, this implies that $P_{\mathrm{abs,non-lin}}$ reaches a global minimum for $q_2 = -q_1/\sqrt{3}$. The corresponding maximum and squirmer parameter are

$$\epsilon^{\star}_{\mathrm{non-lin}} = \frac{3\sqrt{3}}{2}\frac{\eta\chi}{aT_0}\frac{U}{\kappa_{\mathrm{in}} + 2\kappa_{\mathrm{out}}} = \frac{2}{\sqrt{3}}\epsilon^{\star}_{\mathrm{lin}}\,, \tag{S76}$$

$$\beta^{\star}_{\mathrm{non-lin}} = -\sqrt{3}\frac{\kappa_{\mathrm{in}} + 2\kappa_{\mathrm{out}}}{2\kappa_{\mathrm{in}} + 3\kappa_{\mathrm{out}}} = \sqrt{3}\beta^{\star}_{\mathrm{lin}}\,. \tag{S77}$$

In the quadrupole approximation, the most efficient non-linear swimmer is thus more efficient than the most efficient linear swimmer. Both optimal swimmers are pushers ($\beta < 0$). This is consistent with the temperature measurements (cf. Fig. S**5**d), which show that the pusher exhibits the lowest surface temperature. For typical values of $\kappa_{\mathrm{in}} = 0.03\,\mathrm{W}\,(\mathrm{m\,K})^{-1}$ and $\kappa_{\mathrm{out}} = 0.15\,\mathrm{W}\,(\mathrm{m\,K})^{-1}$, we find $\beta^{\star}_{\mathrm{lin}} = -0.64$ and $\beta^{\star}_{\mathrm{non-lin}} = -1.12$.

S5.3 Optimal heating and maximum efficiency beyond the quadrupole approximation

Let us now find the optimal heating pattern for a given propulsion speed $U \sim -q_1 > 0$ without relying to the quadrupole approximation.

For the given axial symmetry of illumination profiles, an arbitrary heat flux density can be constructed from circular illumination profiles around the propulsion axis. Such profiles correspond to heat flux density $q(\theta)$ given by a delta function $q(\theta) = A\delta(\cos\theta - \cos\theta_0)$, with θ_0 measuring the distance of the circle from the pole of the particle in the propulsion direction.

The general heat source expansion is

$$q(\theta) = \sum_{l=0}^{\infty} q_l P_l(\cos\theta)\,. \tag{S78}$$

Using the orthogonality of the Legendre polynomials ($\int_{-1}^{1} P_l(x)P_m(x)dx = \frac{l}{2l+1}\delta_{lm}$) with $x = \cos\theta$ so that $dx = -\sin\theta d\theta$ ($\theta \in [0,\pi]$ and $x \in [-1,1]$), we obtain the expansion coefficients

$$q_l = \frac{2l+1}{2}\int_0^{\pi} q(\theta)P_l(\cos\theta)\sin\theta d\theta\,. \tag{S79}$$

For a delta function $q(\theta) = A\delta(\cos\theta - \cos\theta_0)$ at arbitrary angle θ_0, the Legendre coefficients are then

$$q_l = \frac{2l+1}{2} A P_l(\cos\theta_0)\,. \tag{S80}$$

The monopole, dipole, and quadrupole heating contributions are $q_0 = \frac{A}{2}$, $q_1 = \frac{3A}{2}\cos\theta_0$, and $q_2 = \frac{5A}{2}\frac{3\cos^2\theta_0 - 1}{2}$, respectively. In this case, the condition of positive heating everywhere is trivially satisfied for $A > 0$.
To achieve a fixed propulsion velocity, the dipole heating q_1 is held constant. We thus have $A = \frac{2q_1}{3\cos\theta_0}$ and

$$q_0 = \frac{A}{2} = \frac{q_1}{3\cos\theta_0}\,. \tag{S81}$$

For an optimal swimming efficiency, the monopole heating should be minimized under the condition $q_0 > 0$. For a fixed $q_1 < 0$, we thus minimize $\cos\theta_0$:

$$\cos\theta_0^{\text{opti}} = -1 \Longleftrightarrow \theta_0^{\text{opti}} = \pi\,. \tag{S82}$$

This means that the most efficient way to produce a given propulsion speed $U \sim -q_1$ is to concentrate all heating into a localized spot at $\theta_0^{\text{opti}} = \pi$, i.e., at the pole opposite to the propulsion direction. Dividing the overall heating power into several rings at different azimuthal angles, or creating more complicated illumination profiles, can only decrease the efficiency.
The corresponding maximum swimming efficiency and squirmer parameter are

$$\epsilon_\infty^\star = \frac{9}{2}\frac{\eta\chi}{aT_0}\frac{U}{\kappa_{\text{in}} + 2\kappa_{\text{out}}} = 2\epsilon_{\text{lin}}^\star\,, \tag{S83}$$

$$\beta_\infty^\star = -5\frac{\kappa_{\text{in}} + 2\kappa_{\text{out}}}{2\kappa_{\text{in}} + 3\kappa_{\text{out}}} = 5\beta_{\text{lin}}^\star\,. \tag{S84}$$

The most efficient swimmer is therefore more efficient than the best linear swimmer in the quadrupole approximation by a factor of 2, and than the best non-linear swimmer in the quadrupole approximation by a factor of $\sqrt{3} \approx 1.73$. Its squirmer parameter is substantially more negative than that of both swimmers in the quadrupole approximation—by a factor of five compared to the linear case and by a factor of three compared to the nonlinear case—indicating that it is a markedly stronger pusher.

Supplementary References

[1] Lighthill, M. J. On the squirming motion of nearly spherical deformable bodies through liquids at very small reynolds numbers. *Communications on pure and applied mathematics* **5**, 109–118 (1952).

[2] Horn, R. G. Refractive indices and order parameters of two liquid crystals. *Journal de physique* **39**, 105–109 (1978).

[3] Baffou, G., Quidant, R. & Girard, C. Thermoplasmonics modeling: A green's function approach. *Physical Review B—Condensed Matter and Materials Physics* **82**, 165424 (2010).

[4] Rohde, L., Quinn, D., Paul, D. & Cichos, F. Regulated polarization of active particles in local osmotic flow fields. *Communications Physics* **8**, 213 (2025).